Journal of the European Ceramic Society 43 (2023) 1548–1558

Contents lists available at ScienceDirect

Journal of the European Ceramic Society

journal homepage: www.elsevier.com/locate/jeurceramsoc

Symmetrical solid oxide fuel cells based on titanate nanocomposite electrodes

Javier Zamudio-García [a], Lucía dos Santos-Gómez [a], José Manuel Porras-Vázquez [a], Enrique R. Losilla [a], David Marrero-López [b,*,1]

[a] Universidad de Málaga, Departamento de Química Inorgánica, 29071 Málaga, Spain
[b] Universidad de Málaga, Departamento de Física Aplicada I, 29071 Málaga, Spain

ARTICLE INFO

Keywords:
SOFC
$SrTiO_3$
CeO_2
Symmetrical electrode
Nanocomposite

ABSTRACT

Nanocomposite electrodes of $(Sr_{0.7}Pr_{0.3})_{0.95}TiO_{3\pm\delta}$–$Ce_{0.9}Gd_{0.1}O_{1.95}$ are directly prepared by spray-pyrolysis deposition on $Zr_{0.82}Y_{0.16}O_{1.92}$ electrolytes and their properties are compared with those obtained by the traditional screen-printing powder method. The structural, microstructural and electrical characteristics are investigated for their potential use as both cathode and anode in Solid Oxide Fuel Cells. The nanocomposite electrodes with reduced particle size ~30 nm achieved a polarization resistance at 700 ºC of 0.50 and 0.46 Ω cm^2 in air and pure H_2, respectively, outperforming those obtained for the analogous screen-printed electrodes with particle size of 450 nm, i.e. 4.8 and 3.9 Ω cm^2, respectively. An electrolyte-supported cell with symmetrical electrodes reached a maximum and stable power density of 354 mW cm^{-2} at 800 ºC. These results demonstrate that the performance of electrode materials with modest electrochemical properties but high phase stability, such as doped-$SrTiO_3$, can be highly improved by preparing nanocomposite electrodes directly on the electrolyte surface.

1. Introduction

Nowadays, Solid Oxide Fuel Cells (SOFCs) are considered as one of the most promising and efficient technologies for electricity generation from a wide variety of fuel gases, such as hydrogen or hydrocarbons [1,2]. However, their commercialization is still hindered by several issues, such as high manufacturing and maintenance costs, as well as short durability of the cell components at high operation temperature.

In particular, the traditional Ni-based cermet anodes, suffer from thermomechanical stability upon redox cycles due to Ni agglomeration and they are prone to coking and sulphur poisoning, leading to degradation of the microstructure and loss of performance under long-term operation [3,4]. Several mixed oxide anodes with perovskite-type structure have been investigated to overcome these issues, such as $La_{0.75}Sr_{0.25}Cr_{0.5}Mn_{0.5}O_{3-\delta}$ [5], $Sr_2MgMoO_{6-\delta}$ [6,7], $Sr_2Fe_{1.5}Mo_{0.5}O_{6-\delta}$ [8] or $PrBa(Fe,Mn)_2O_{5+\delta}$ [9]. Moreover, these electrodes have been also tested in symmetrical solid oxide fuel cells (SSOFCs), in which the same electrode material is employed simultaneously as both air and fuel electrode [10].

Among the different anode materials, doped-$SrTiO_3$ are highly attractive because of their exceptional stability under both oxidizing and reducing conditions, moderate thermal expansion, as well as high tolerance to sulphur and carbon deposition [11,12]. Furthermore, strontium titanates are chemically compatible with the most widely used solid electrolytes up to 1400 ºC, such as $Zr_{0.82}Y_{0.16}O_{1.92}$ (YSZ), $La_{0.9}Sr_{0.1}Ga_{0.8}Mg_{0.2}O_{3-\delta}$ (LSGM) and $Ce_{0.9}Gd_{0.1}O_{1.95}$ (CGO) [13]. However, the performance of strontium titanates is rather modest compared to the state-of-the-art anode materials due to their poor ionic conductivity and electrocatalytic activity.

The electrochemical properties of $SrTiO_{3\pm\delta}$ are usually improved by doping with higher valence cations, such as rare-earth elements (La^{3+}, Pr^{3+}, Nd^{3+} and Y^{3+}) in the Sr-site [14–16] or Nb^{5+} in the Ti-site [17]. These materials exhibit high electronic conductivity in reducing atmospheres due to the Ti^{4+}/Ti^{3+} redox couple but the conductivity is relatively low in oxidizing conditions. The oxygen non-stoichiometry, δ, also plays a critical role in both structural and electrochemical properties. In particular, layered perovskite related phases with poor electrochemical properties have been observed by increasing the lattice oxygen content [18,19]. Furthermore, significant differences in the conductivity values are reported in the literature, suggesting that the electronic conductivity

* Corresponding author.
E-mail address: marrero@uma.es (D. Marrero-López).
[1] Present address: Dpto. de Física Aplicada I, Facultad de Ciencias, Campus de Teatinos, Universidad de Málaga, 29071-Málaga, Spain.

https://doi.org/10.1016/j.jeurceramsoc.2022.11.059
Received 3 October 2022; Received in revised form 22 November 2022; Accepted 25 November 2022
Available online 26 November 2022

is strongly affected by the synthesis route and the thermal treatment employed [20].

Pr-doped $SrTiO_{3\pm\delta}$ has been previously studied for potential application as SOFC anode [21,22]. The presence of mixed Pr^{4+}/Pr^{3+} with high electrocatalytic activity for the oxygen reduction reaction has a great influence on the electrical properties of $SrTiO_{3\pm\delta}$. For instance, Yaremchenko et al. [21] reported conductivity values of 0.1 and 10 S cm^{-1} at 800 ºC for $Sr_{0.7}Pr_{0.3}TiO_{3\pm\delta}$ in air and 10% H_2-N_2, respectively, making this composition highly attractive for potential application as symmetrical electrode for both oxygen reduction reaction (ORR) and hydrogen oxidation reaction (HOR) [23–25].

The electrochemical properties of $SrTiO_3$−based electrodes have also been improved by using different strategies, i.e. by making composites with CeO_2 ionic conductors [26,27] or by infiltration with catalytic active materials, such as Ni and noble metals [28,29]. However, the performance is still rather poor for their implementation in SOFCs.

Recently, the electrochemical performance of conventional air electrodes, such as $La_{0.8}Sr_{0.2}MnO_{3-\delta}$ (LSM) and $La_{0.6}Sr_{0.4}Co_{0.2}Fe_{0.8}O_{3-\delta}$ (LSCF), have been greatly improved by preparing nanocomposite materials with $Ce_{0.9}Gd_{0.1}O_{1.95}$ (CGO) [30–32]. The nanocomposite electrodes showed very low grain size because CGO addition partially suppresses the particle growth at high sintering temperatures, obtaining electrodes with extended active sites for the ORR. More recently, $LaCrO_3$−CeO_2 nanocomposites were investigated as symmetrical electrodes [33], achieving low polarization resistance values of 0.29 and 0.09 Ω cm^2 at 750 °C in air and H_2, respectively. The great improvement in H_2 was attributed to the better activity of the nanostructured electrodes and the presence of reduced nano-CeO_2, which have demonstrated excellent properties for different electrocatalytic processes [34,35]. Based on these previous studies, Pr-doped $SrTiO_{3\pm\delta}$ could be combined with CGO to obtain new nanocomposite electrodes with high redox stability and improved electrochemical performance for both ORR and HOR in symmetrical SOFCs.

In this work, $(Sr_{0.7}Pr_{0.3})_{0.95}TiO_{3\pm\delta}$ −$Ce_{0.9}Gd_{0.1}O_{1.95}$ (SPTO−CGO) electrodes with different SPTO content are prepared by different methods. i) The electrodes are directly deposited and assembled in situ on the electrolyte surface by spray-pyrolysis deposition at a low temperature of 450 ºC. The electrodes are deposited by traditional screen-printing deposition and sintered at 1100 ºC from ii) mechanically mixed powders of SPTO and CGO and iii) powders obtained by one-step co-synthesis method from freeze-dried precursors. The relevant properties for SOFC applications are investigated, including crystal structure, microstructure, stability upon redox cycles and electrochemical properties under different atmospheres.

2. Experimental

2.1. Materials preparation

The basic electrochemical studies were performed on $Zr_{0.84}Y_{0.16}O_{1.92}$ (YSZ) electrolyte substrates, which were prepared from commercial powders supplied by Tosoh Co. Ltd. The powders were pressed into disks (10 mm diameter and 1 mm thickness) and sintered at 1400 ºC for 4 h to obtain full dense pellets.

Nanocomposite electrodes with nominal composition x $(Sr_{0.7}Pr_{0.3})_{0.95}TiO_3$–(100-x) $Ce_{0.9}Gd_{0.1}O_{1.95}$ (x = 40, 50 and 60 wt%) were deposited in a single step by spray-pyrolysis on YSZ pellets. Notice that the electrode materials were A-site deficient to prevent possible Sr-segregation. Hereafter, the spray-pyrolysis electrodes are denoted as *x*SPTO, where *x* represents the amount of SPTO in wt%.

The precursor solutions were obtained by dissolving in Milli-Q water, stoichiometric amounts of $Sr(NO_3)_2$, $Pr(NO_3)_3{\cdot}6H_2O$, $Ti[OCH(CH_3)_2]_4$, $Ce(NO_3)_3{\cdot}6H_2O$ and $Gd(NO_3)_3{\cdot}6H_2O$ (all supplied by Merck and purity above 99%). Ethylenediamine-tetraacetic acid (EDTA) was used as a complexing agent to stabilize the cation solutions in a ligand:metal molar ratio of 0.5:1. The titanium (IV) isopropoxide solution was prepared separately by weighing in absolute ethanol and adding the EDTA solution. The cation solutions were mixed to obtain a light yellow and transparent solution with a final cation concentration of 0.02 mol L^{-1} for all compositions.

The precursor solutions were sprayed at a flow rate of 20 mL h^{-1} through a conventional spray nozzle on the YSZ pellet surface at 450 ºC for 1 h with an air pressure of 2 bars. Further experimental details about the spray-pyrolysis equipment can be found elsewhere [33]. Afterwards, the layers were sintered in air at 800 ºC for 1 h to achieve crystallization.

The composite electrodes were also deposited by the traditional screen-printing method by using two different approaches to demonstrate the advantage of the spray-pyrolysis deposition over screen-printing deposition. In the first approach, SPTO and CGO powders were synthesized separately by using a freeze-dried precursor method. The cation solutions with a concentration of 0.1 mol L^{-1} were prepared from the same reagents used for the spray-pyrolysis deposition. After that, the precursor solutions were frozen into liquid nitrogen and then freeze-dried for 2 days. The resulting dried precursors were calcined in air at 800 ºC for 1 h. The SPTO and CGO crystalline powders were physically mixed in 50 wt% by using Decoflux™ as organic binder, and the resulting ink was screen-printed onto the YSZ electrolyte and sintered at 1100 ºC for 1 h to ensure sufficient adhesion to the electrolyte.

In a second approach, the same SPTO-CGO composite electrode was prepared in one-step by the freeze-drying method from a precursor solution containing all cations in stoichiometric amounts. Similarly, the powders were calcined at 800 ºC, screen-printed on the YSZ electrolyte and then sintered at 1100 ºC for 1 h.

The screen-printed powders electrodes with 50 wt% SPTO, obtained by physically mixed powders (PM) and co-synthesis by freeze-drying (FD), will be denoted as 50SPTO-PM and 50SPTO-FD, respectively. The blank SPTO electrode, obtained from freeze-drying, will be labelled as 100SPTO-FD (Table S1).

2.2. Structural and microstructural characterization

The structure and composition were studied by X-ray diffraction (XRD) with an Empyrean PANalytical diffractometer using $CuK_{\alpha1,2}$ radiation. The XRD patterns were analyzed with the Highscore Plus software and refined by the Rietveld method using the GSAS program [36,37]. During the fitting process, the scale factor, background, zero shift, peak-shape asymmetry and preferential orientation were refined, and the cation occupation factors were fixed to the nominal values.

The morphology was inspected by scanning electron microscopy (SEM) in a FEI-SEM (Helios Nanolab 650) coupled with energy dispersive spectroscopy (EDS, X-Max, Oxford instruments). The grain size distribution was determined by the linear intercept method [38]. The local crystal structure and elemental composition were examined by High-Angle Annular Dark-Field Scanning Transmission Electron Microscopy (HAADF-STEM) and High-Resolution TEM (HR-TEM) in a FEI Talos F200X.

2.3. Electrochemical characterization

The electrical conductivity of the electrodes was determined by the four-probe Van der Pauw method as a function of the temperature in controlled atmospheres [39]. Pellets of 13 and 1 mm in diameter and thickness, respectively, were prepared by pressing the powders in a die and then sintered at 1500 ºC for 1 h for 100SPTO-FD and 1400 ºC for 1 h for both 50SPTO-FD and 50SPTO-PM, reaching relative densities above 95%. The conductivity of the pellets was determined in air and 5% H_2-Ar on cooling in the temperature range of 750–450 ºC, as well as during several redox cycles by switching between air and 5% H_2-Ar.

The electrode polarization resistance was determined by electrochemical impedance spectroscopy (EIS) in symmetrical cell configuration at open circuit voltage. Pt-paste (METALOR® 6082) was painted on the electrode surface and then calcined at 750 ºC for 30 min to obtain a

current collector layer. The EIS measurements were performed with a Solartron 1260 FRA with an AC amplitude of 50 mV in the frequency range of 10^{-2}-10^{6} Hz in static air and pure H_2 with a flow rate of 10 mL min^{-1}. The data were acquired on cooling from 750 to 450 °C with a dwell time of 1 h at each temperature. The impedance spectra were also acquired as a function of the oxygen partial pressure to identify the electrochemical processes involved in the ORR [40]. The EIS data were fitted with ZView software using equivalent circuit models (Scribner Associates). Distribution of relaxation times (DRT) was previously used to elucidate the different processes involved in the EIS data [41].

Symmetrical cells with configuration: 50SPTO / LSGM / 50SPTO were assembled for fuel cell test. $La_{0.9}Sr_{0.1}Ga_{0.8}Mg_{0.2}O_{3-\delta}$ (LSGM) electrolyte was used instead of YSZ due to its higher ionic conductivity at intermediate temperature, decreasing the ohmic losses of the cell. $La_{0.9}Sr_{0.1}Ga_{0.8}Mg_{0.2}O_{3-\delta}$ (Kceracell) pellets of 13 mm diameter and 300 μm thickness were sintered at 1400 °C for 4 h in air. 50SPTO was deposited symmetrically by spray-pyrolysis at 450 °C onto both sides of LSGM pellets through circular shadow mask of 0.25 cm^2 and then calcined at 800 °C. For comparison purposes, a similar cell with screen-printed electrodes (50SPTO-PM) was also prepared at 1100 °C. The fuel cells were sealed by using a high temperature ceramic adhesive (Ceramabond 668, Aremco). Current-voltage curves were collected using a Zahner XC potentiostat/galvanostat/impedance analyzer at various temperatures between 800 and 700 °C. The anode side was fueled with humidified H_2 (3% H_2O) at a flow rate of 20 mL min^{-1}, while the cathode side was exposed to static air.

3. Results and discussion

3.1. Structural characterization

The XRD patterns indicate that the powders of SPTO and CGO, obtained by the freeze-drying method, are single phase materials at 800 °C (Fig. 1a). The SPTO and CGO phases are adequately refined in the cubic perovskite *Pm-3 m* and cubic fluorite *Fm-3 m* space groups, respectively (Fig. S1a, S1b and Table S1). The biphasic 50SPTO-FD powders are also successfully synthesized in one-step by the freeze-drying method at 800 °C (Fig. S1c). However, the unit cell volumes of the constituent phases are slightly different when compared to the single-phase electrode, suggesting cation exchange during the co-synthesis process (Table S1). This fact is not surprising considering the similarities between the rare-earth elements, such as valence state and ionic radii: r(Ce^{4+})= 0.97 Å, r(Pr^{4+})= 0.96 Å, r(Pr^{3+})= 1.126 Å, Sr^{2+} (1.26 Å) and r(Gd^{3+})= 1.053 Å in eightfold coordination [42]. In this context, previous studies demonstrated a low solubility of Gd in $Sr_{1-x}Gd_xTiO_3$ ($x < 0.1$) due to the smaller ionic radii of Gd^{3+}, which leads to the formation of $Gd_2Ti_2O_7$ as secondary phase [43,44]. On the contrary, high Pr-content ($x \leq 0.3$) was successfully incorporated in the A-site of $Sr_{1-x}Pr_xTiO_{3-\delta}$ [21,22], while Ce showed a very low solubility in $Sr_{1-x}Ce_xTiO_{3-\delta}$, estimated to be $x = 0.03$ by XRD [45]. These secondary phases are not observed in the XRD patterns even at 1400 °C (Fig. S1d), confirming minor cation exchange between SPTO and CGO phases.

The XRD patterns of SPTO-CGO layers with different SPTO content, deposited by spray pyrolysis on YSZ pellets, are shown in Fig. 1b. The diffraction peaks of three different phases are clearly discernible, which are assigned to SPTO (s.g. *Pm-3m*), CGO (s.g. *Fm-3m*) and YSZ substrate (s.g. *Fm-3m*). Notice that additional diffractions peaks, attributed to secondary phases, are not visible even after calcining at 1000 °C for 12 h in both air and 5% H_2-Ar. A representative Rietveld plot for 50SPTO is shown in Fig. 1c. The R_{wp} disagreement factor varies between 3.4% and 9.5%, indicating a good fitting of the experimental data. It is also worth noting that the phase fraction is almost identical to the nominal ones (Table S1).

Moreover, similar lattice parameters were obtained, regardless of the composition of the nanocomposite layers. For instance, the unit cell volume of the SPTO constituent takes values in the range of 59.338(2)–59.591(2) $Å^3$, which is somewhat larger than that found for the corresponding powder material 59.128(3) $Å^3$ at 800 °C. A similar trend was observed for the CGO constituent, varying from 157.577(2) $Å^3$ for 40SPTO to 157.873(2) $Å^3$ for 60SPTO, which are somewhat lower than those obtained for CGO powders 159.202(4) $Å^3$, indicating certain cation exchange between the phase constituents, but without reaction product formation.

On the other hand, the unit cell volume of SPTO seems to be strongly dependent on the annealing temperature, increasing from 59.128(3) $Å^3$ at 800 °C to 59.659(3) $Å^3$ at 1500 °C for 100SPTO-FD (Table S1), which is possibly related to changes in the Pr^{3+}/Pr^{4+} ratio, the formation of additional defects, as well as variation of the lattice oxygen stoichiometry [46]. In addition, the unit cell volume of SPTO does not change appreciably in reducing atmosphere in agreement to previous studies [14,21].

The crystallite size, estimated using the Scherrer's formula, is clearly smaller for the nanocomposite layers with values as low as 14 and 8 nm for the SPTO and CGO, respectively, at 800 °C. More interestingly, the

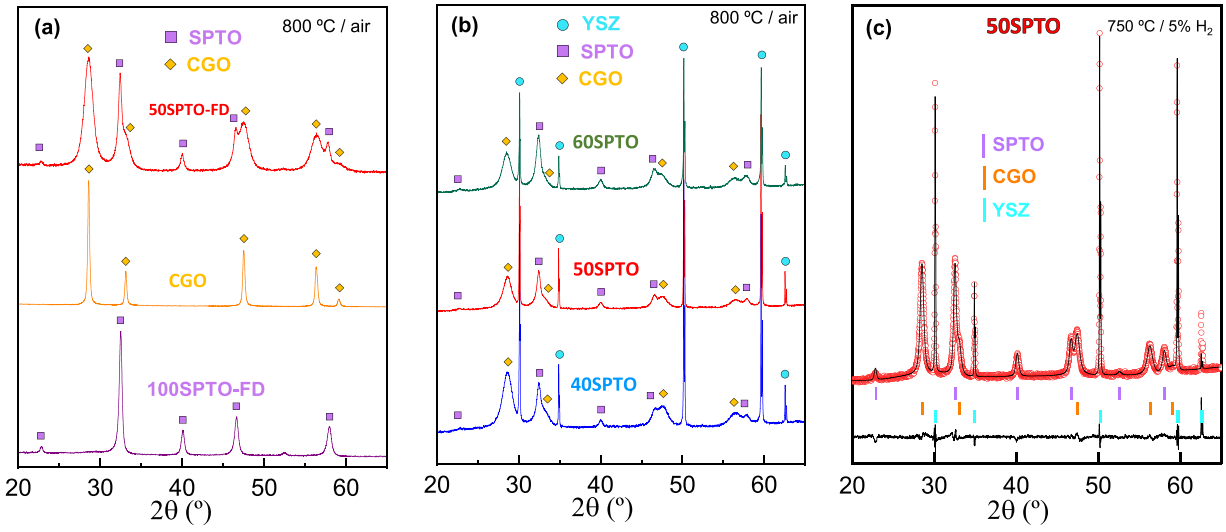

Fig. 1. (a) XRD patterns of $(Sr_{0.7}Pr_{0.3})_{0.95}TiO_3$ (SPTO), $Ce_{0.9}Gd_{0.1}O_{1.95}$ (CGO) and 50 wt% SPTO-CGO composite powders (50SPTO-FD) prepared by freeze-dried precursors at 800 °C in air. (b) XRD patterns of SPTO-CGO composite layers with different SPTO content (40, 50 and 60 wt%) deposited by spray-pyrolysis on YSZ electrolyte and sintered at 800 °C for 1 h in air. (c) Rietveld plot of 50SPTO. The main diffraction peaks of the different phases are indicated with symbols.

average crystal size is lower than 25 nm even after annealing at 1000 ºC (Table S1). This effect is clearly attributed to the intimate mixture of two immiscible SPTO and CGO phases, which hinders the grain growth due to cation diffusion limitations at the grain boundary region [37].

TEM and EDS analysis were performed to get further information about the local crystal structure and composition of the electrodes. EDS analysis of 100SPTO-FD powders confirms a homogenous distribution of elements (Fig. S2). Furthermore, the d-spacing or lattice spacing for the different crystallographic planes are consistent with those obtained from XRD Rietveld method.

The nanocomposite electrodes, obtained by spray-pyrolysis at 800 ºC, consist of a homogeneous mixture of SPTO and CGO particles (Fig. 2a). The particles with a diameter lower than 10 nm are highly crystalline and present an intimate contact between them (Fig. 2b). Hence, this electrode architecture ensures a high percolation and contact area between both SPTO and CGO phases, which is expected to improve the electrochemical properties for both ORR and HOR. Furthermore, the grain size and d-spacings for the different crystals match well with those obtained from XRD data (Table S1).

The increase of the annealing temperature up to 1000 ºC leads to grain growth and a different atomic arrangement is visible in some SPTO crystals (Fig. 2c). In particular, layered ordered extended defects are observed, which are reported to be detrimental for the electrical properties of strontium titanates [18]. Interestingly, the HRTEM results suggest that these ordered domains are not present for those samples prepared at low sintering temperature, possibly due to the smaller crystal size, which hinders their formation.

3.2. Microstructural characterization

The microstructure of the electrodes prepared by spray-pyrolysis and screen-printing deposition is compared in Fig. 3. The spray-pyrolysis electrode, 50SPTO, shows a laminated morphology with an average thickness of approximately 7 μm, as well as a strong adhesion to the YSZ substrate after successive oxidation/reduction cycles (Fig. 3a).

It is also worth noting that the thermal expansion coefficients of Pr-doped $SrTiO_3$ ($11.7–12.3{\cdot}10^{-6}$ K^{-1} for $Sr_{0.8}Pr_{0.2}TiO_{3\pm\delta}$ in both air and H_2 [21]) are comparable to those reported for conventional electrolytes: YSZ ($10.9{\cdot}10^{-6}$ K^{-1}), CGO ($12.7{\cdot}10^{-6}$ K^{-1}) and LSGM ($11.4{\cdot}10^{-6}$ K^{-1}) [21, 47]. This guarantees a good mechanical compatibility of these electrodes with the electrolyte, avoiding delamination of the cell layers upon redox cycles.

More interestingly, the particle size is maintained at the nanometric scale with a value of approximately 32 nm at 800 ºC (Fig. 3b). Such nanoscale architecture is mainly attributed to the low deposition temperatures, as well as the grain growth suppression in the self-assembled nanocomposite electrodes prepared in a one-step directly on YSZ electrolyte.

The screen-printed electrodes, obtained by powder mixture (50SPTO-PM) and co-synthesis process via freeze-drying (50SPTO-FD), have a thickness of approximately 15 μm (Figs. 3c and 3e). The most remarkable difference between both electrodes is the different grain size with values of 450 nm for 50SPTO-PM and 58 nm for 50SPTO-FD nm at the same sintering temperature of 1100 ºC (Figs. 3d and 3f). This further confirms that a homogeneous and intimate mixture of SPTO and CGO phases impedes the grain growth during the sintering process [33,48]. Nevertheless, 50SPTO-FD consists of highly aggregated nanoparticles, resulting in a drastic reduction of the active surface area when compared to the same electrode directly deposited by spray-pyrolysis on the electrolyte surface. Thus, the spray-pyrolysis nanocomposite electrodes with increased gas/solid interface are expected to exhibit faster reduction kinetics and improved electrochemical properties.

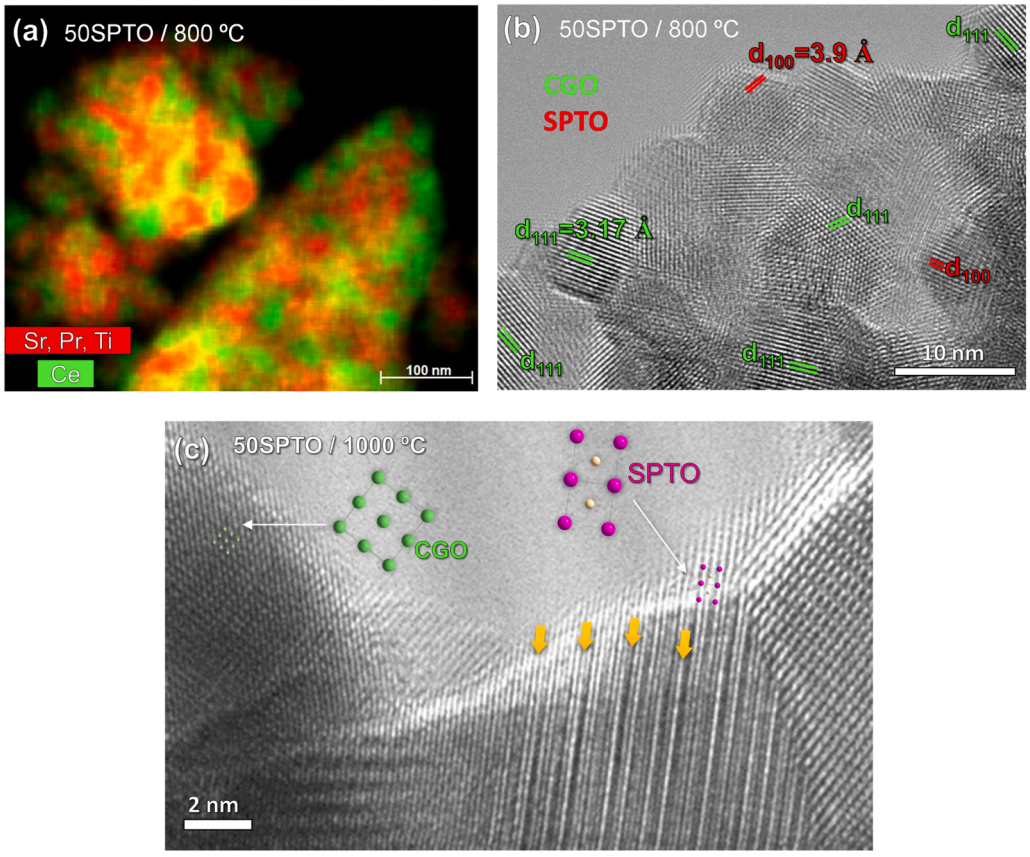

Fig. 2. (a) HAADF-EDS image of 50SPTO sintered at 800 ºC and (b) HRTEM showing a homogenous mixture of SPTO and CGO particles. (c) HRTEM of 50SPTO sintered in air at 1000 ºC, showing ordered extended defects for SPTO phase.

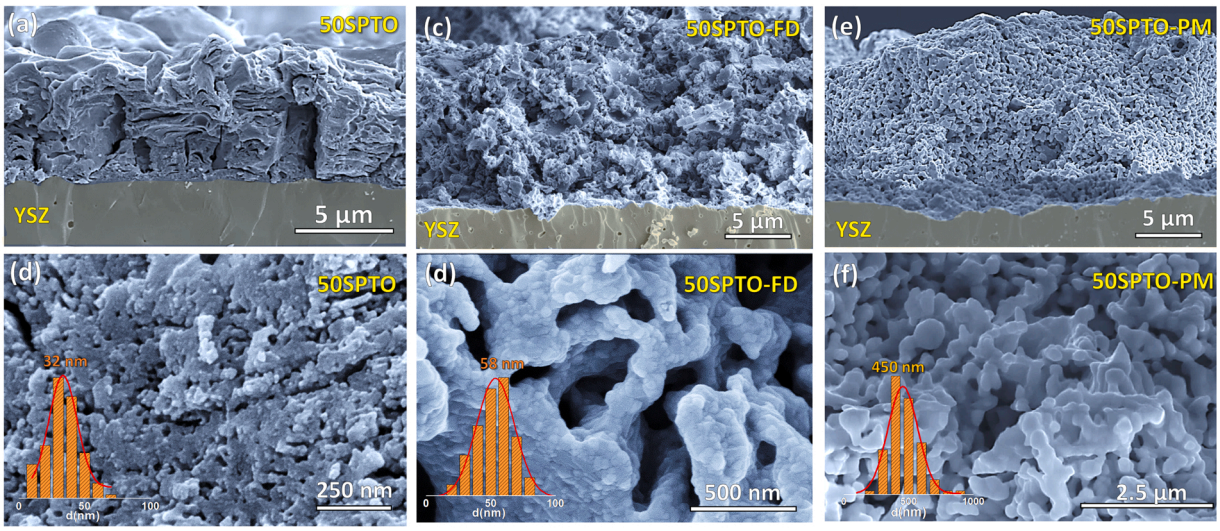

Fig. 3. SEM image of 50SPTO prepared by (a-b) spray pyrolysis deposition on YSZ electrolyte at 800 ºC, (c-d) screen-printed powders obtained by co-sintering method at 1100 ºC and (e-f) screen-printed powders obtained by milling mixture of SPTO and CGO powders at 1100 ºC.

3.3. Electrical conductivity

The microstructure of the sintered pellets, 100SPTO-FD, 50SPTO-PM and 50SPTO-FD, for electrical conductivity determination are shown in Figs. 4a-4c. All pellets exhibit similar relative densities above 95% after sintering at 1500 ºC for pure 100SPTO-FD and 1400 ºC for the composite pellets. The average grain size depends on the composition and the preparation method employed. 100SPTO-FD has a grain size of 1.25 µm and the EDS analysis confirm a homogenous cation distribution without detectable phase segregations (Fig. 4a). In the case of the composite electrodes, two well-differentiated phases are discernible. 50SPTO-PM, obtained by physically mixed powders, exhibits a non-homogeneous grain size distribution of approximately 1 µm diameter (Fig. 4b). Interestingly, the co-synthesis electrode, 50SPTO-FD, shows a more homogenous grain size and phase distribution, as well as smaller grain size of 0.5 µm when compared to the analogous pellet obtained from physically mixed powders (Fig. 4c).

Fig. 4d compares the electrical conductivity as a function of the temperature for the different samples. The conductivity in air for 100SPTO-FD is relatively low, $5.9{\cdot}10^{-5}$ S cm^{-1} at 700 ºC, since the concentration of charge carriers in these materials is considered proportional to the concentration of Ti^{3+}, which is unlikely under oxidizing conditions. In addition, the minor contribution of the Pr^{3+}/Pr^{4+} couple to the electronic conductivity seems to be not significant. The conductivity values for similar compositions reported in the literature vary in a broad range from $2{\cdot}10^{-5}$ S cm^{-1} for $Sr_{0.7}Pr_{0.3}Ti_{0.93}Co_{0.07}O_{3-\delta}$ to ~10^{-2} S cm^{-1} at 700 ºC for $Sr_{0.8}Pr_{0.2}TiO_{3-\delta}$ [21,46]. Such differences are explained by the different preparation conditions, i.e. temperature, time and atmosphere pre-treatment. Previous studies for $Sr_{1-x}Pr_xTiO_{3-\delta}$ series also confirmed by thermogravimetric and thermopower analysis that the concentration of charge carriers in oxidizing conditions is nearly constant and the level of electrical conductivity is determined by the Pr-content [21]. The electronic conductivity increases initially with Pr-content, reaching a maximum for x ~0.15 [46], and above this substitution level the conductivity decreases due to possible formation of linear defect clusters. In particular, Ruddlesden–Popper phases are the most probable extended defects, enabling the accommodation of oxygen excess in rare-earth doped titanates, which are reported to diminish the charge carrier concentration and limit their mobility [21, 49].

In reducing atmosphere (5% H_2-Ar), the conductivity of 100STPO-FD increases considerably with respect to air, reaching a value of 1.18 S cm^{-1} at 700 ºC, which is mainly associated with the partial reduction of Ti^{4+} to Ti^{3+}. It has to be also commented that the conductivity values determined in the present study are lower than those reported by Yaremchenko et al. for a similar composition $Sr_{0.7}Pr_{0.3}TiO_{3\pm\delta}$, e.g. ~10 S cm^{-1} at 700 ºC [21]. Such differences are explained by the different synthetic method employed and thermal pretreatment of the samples. Yaremchenko et al. prepared the samples by traditional solid state reaction at 1600 ºC in air and then reduced at 1500 ºC for 10 h in 10% H_2-N_2, leading to the formation of additional crystal defects, which further enhances the electronic conductivity [21]. In fact, it has been reported that the defect equilibrium in strontium titanates is nearly frozen at temperatures below 1200 ºC and thus the electrical properties are strongly determined by the thermal pre-treatment [50].

The composite electrodes exhibit similar conductivity in air ~$6{\cdot}10^{-3}$ S cm^{-1} at 700 ºC for both samples prepared by mixed powders (50SPTO-PM) and co-synthesis method (50SPTO-FD). The increase of conductivity with respect to the blank sample, 100SPTO-FD, is attributed to the presence of the CGO phase that provides additional ionic conductivity.

In reducing atmosphere, the conductivity of 50SPTO-FD is somewhat higher than that of 50SPTO-PM, especially at low temperature, reaching a value of 0.27 S cm^{-1} at 700 ºC. As expected, the values of conductivity are clearly inferior, compared to the blank 100SPTO-FD, due to the much lower electronic contribution of CGO under reducing atmosphere.

The variation of the conductivity with the oxygen partial pressure (pO_2) indicates that 100SPTO-FD is an n-type electronic conductor with low ionic contribution to the total conductivity (Fig. 4e). The conductivity follows a $(pO_2)^{-1/6}$ dependence in both oxidizing and reducing atmosphere, similar to that predicted by the defect chemistry model in previous studies [21]. The composite electrode, 50SPTO-FD, is a mixed ionic-electronic conductor due to the combination of the electrical properties of CGO and SPTO phases. The conductivity is nearly independent on pO_2 between 0.1 and 10^{-12} atm, indicating a predominant ionic conduction. However, the n-type electronic conductivity becomes the main contribution at lower pO_2 values, following a $(pO_2)^{-1/6}$ dependence similar to that of 100SPTO-FD.

The electrical conductivity and redox stability of 50SPTO-FD were studied for 80 h in consecutive reduction/oxidation cycles at 700 ºC, obtaining reproducible results (Fig. 4f). The dense samples are completely reduced from air to 5% H_2-Ar in approximately 2 h; however, the oxidation kinetics is faster, reaching equilibrium in only 20 min. In comparison to previous studies, the composite electrodes seem to present faster reduction kinetics due to the smaller particle size of the pellets studied in the present work [21].

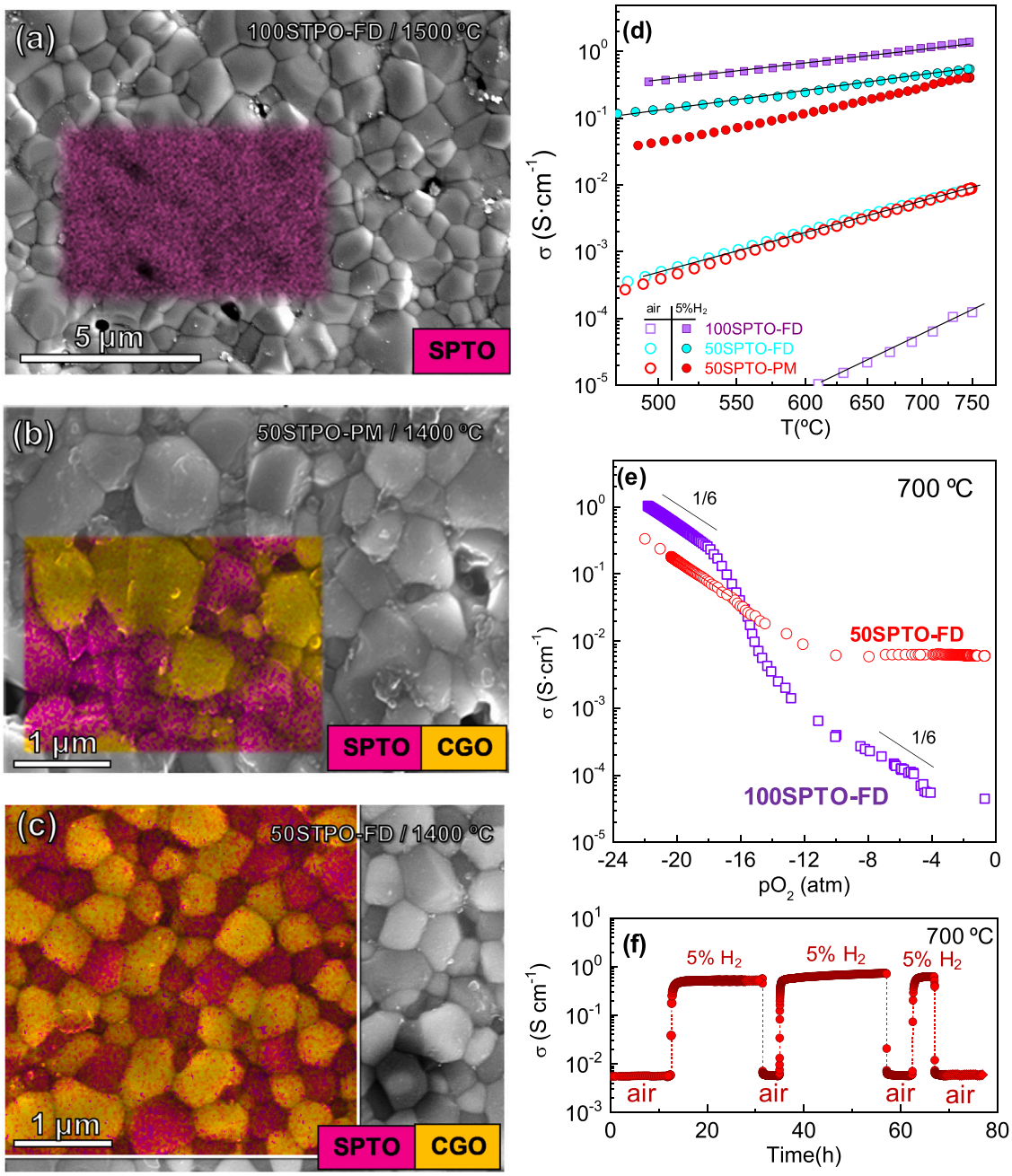

Fig. 4. SEM image of the pellets of (a) 100STPO-FD sintered at 1500 °C for 1 h, (b) 50STPO-PM obtained by mixed powders at 1400 °C for 1 h and (c) 50SPTO-FD powders obtained by co-synthesis method at 1400 °C for 1 h. (d) Temperature dependence of the electrical conductivity in air and 5% H_2-Ar. (e) Oxygen partial pressure dependence of the electrical conductivity of 100STPO-FD and 50STPO-FD. (f) Variation of the conductivity of 50SPTO-FD during several oxidation/reduction cycles between air and 5% H_2-Ar.

3.4. Electrode polarization resistance

The impedance spectra in both air and H_2 atmosphere for some selected symmetrical cells are displayed in Figs. 5a and 5b. Notice that the ohmic resistance (R_Ω), mainly attributed to the thick YSZ electrolyte, was subtracted from the EIS data for a better comparison of the electrode response. In general, the values of R_Ω for all symmetrical cells are comparable to those of a blank YSZ pellet, e.g. 50 Ω cm^{-1} at 700 °C in both air and H_2 atmosphere, suggesting a good adherence of the electrodes to the electrolyte.

The electrode polarization resistance of the nanocomposite electrodes deposited by spray-pyrolysis is substantially lower than that obtained by screen-printing deposition in both oxidizing and reducing atmospheres, reaching a minimum value for 50SPTO.

The EIS data were further analyzed by distribution of relaxation times (DRT) to elucidate the electrochemical processes involved in both ORR and HOR [51–53]. Three main contributions are discernible in the DRT spectra in both air and H_2 (Figs. 5c and 5d). An additional process (HF) appears at very high frequency for the screen-printed electrodes in air (Fig. 5c). Thus, the EIS data are adequately fitted by using an equivalent circuit formed by three or four (RQ) elements in series, where R is a resistance in parallel with a constant phase element Q (inset Fig. 5a).

According to previous studies, the high frequency (HF) contribution in air can be assigned to oxide ion transfer at the electrode/electrolyte interface [54,55], while the electrode contributions at intermediate (IF)

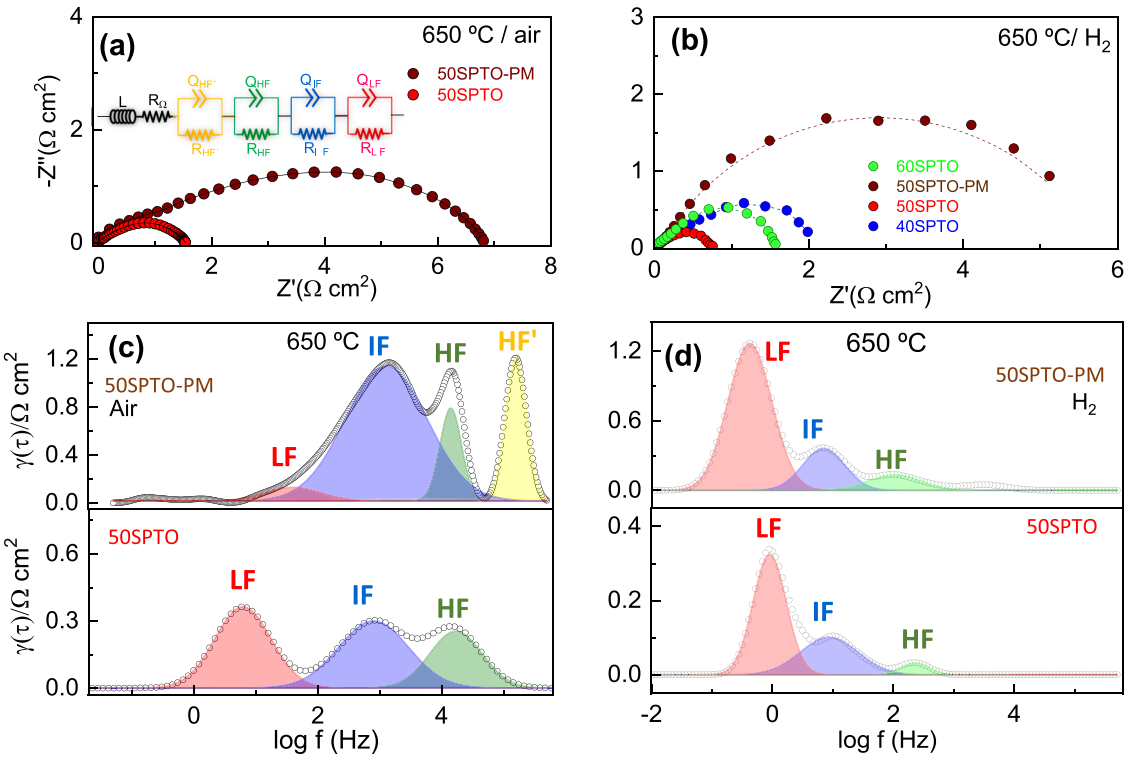

Fig. 5. Impedance spectra of several symmetrical cells at 650 °C in (a) air and (b) H_2. The corresponding DRT spectra for representative samples in (c) air and (d) H_2 with the fitting curves of each peak.

and low frequency (LF) are related to surface electrode processes, such as oxygen dissociation or charge transfer on the electrode surface [51, 54]. These processes are slightly shifted to lower frequency for the nanocomposite electrodes, indicating that they have a higher capacitance due to larger TPB density [56,57]. The HF′ peak, centered at 10^5 Hz for 50SPTO-PM, has been previously assigned to electronic current losses at the current collector/electrode interface [58,59]. This additional resistance can be explained by the poor conducting properties of this electrode in air, which hinders the electronic charge transfer at the current collector/electrode interface. This finding is further corroborated by the fact that this process is not observed in reducing atmosphere due to the enhancement of electronic conductivity.

To further confirm these results, the EIS data were collected at different oxygen partial pressures for 50SPTO (Fig. 6a) and analyzed by DRT method (Fig. 6b). Three different peaks are observed in the DRT spectra and pO_2 range from 10^{-3} to 0.21 atm. The resistance contributions, R_{LF}, R_{IF} and R_{HF}, were determined by deconvolution and integration of the DRT spectra, since the area under each peak is directly proportional to the resistance of each process. The resistance dependence of each process on pO_2 is described by the following equation [60, 61]: $R = R_o\,(pO_2)^{-m}$, where the reaction order m provides information about the species involved in the different ORR steps (Fig. 6c). The LF process is the dominant step at low pO_2 and shows a m close to 1/2, meaning that this process is attributed to oxygen dissociation on the electrode surface: $O_{2,ad} \rightarrow 2O_{ad}$ [62]. Moreover, this process shifts to higher frequency when the pO_2 rises, suggesting that it has a lower relaxation time, and consequently, a faster electrode kinetics. The IF process with $m = 1/4$ is attributed to charge transfer on the electrode surface: $O_{ad} + 2e^- + V_o^{\cdot\cdot} \rightarrow O_o^x$ [63]. Finally, the process at high frequency (HF) is almost pO_2-independent and can be assigned to the oxygen ion transport across the electrode/electrolyte interface: $O_{TPB}^{2-} + V_O^{\bullet\bullet} \rightarrow O_o^x$ [60,63]. This last process is the rate-limiting step for the ORR at high pO_2 values due to the poor ionic conductivity of SPTO in oxidizing atmosphere, hindering the oxide ion transfer to the electrolyte.

In H_2 atmosphere, the LF response is the main contribution to the total electrode polarization resistance for all cells (Fig. 5d). This process decreases significantly when the feeding gas is switched from 5% H_2 to 100% H_2, showing a dependence on the hydrogen partial pressure of $\sim (pH_2)^{-0.8}$, and therefore, it can be attributed to gas diffusion and concentration limitations (Fig. S3) [33]. In contrast, the IF and HF contributions show a weak dependence on H_2 concentration and they are possibly assigned to charge transfer and interfacial processes [51,64].

Fig. 7a compares the total polarization resistance (R_p) in air for the different symmetrical cells. 100SPTO-FD, deposited by screen-printing, exhibits rather high R_p values ~13.6 Ω cm² at 650 °C. The addition of CGO produces a significant reduction of R_p, especially at low temperature, with a value of 6.85 Ω cm² at 650 °C for 50SPTO-PM. Further improvements are observed for the nanocomposite electrodes prepared by spray-pyrolysis deposition, 1.4 Ω cm² for 50SPTO, reaching all compositions R_p values as low as 0.1 Ω cm² at 800 °C, and comparable to those reported for traditional cathodes, e.g. 0.3 Ω cm² at 800 °C for $La_{0.8}Sr_{0.2}MnO_{3-\delta}$ [65]. According to these results, 50STPO is considered the optimal composition, showing the lowest polarization resistance at low temperature, as well as the lowest activation energy ~1.22 eV. It is also worth mentioning that these values of polarization resistance are among the best reported in literature for titanate-based air electrodes, e.g. $La_{1/3}Sr_{2/3}Ti_{0.83}Fe_{0.17}O_{3-\delta}$ (0.5 Ω cm² at 900 °C) [24], $La_{0.875}Sr_{0.125}Ti_{0.5}Ni_{0.5}O_3$ (1.1 Ω cm² at 800 °C) [23], $La_{0.43}Ca_{0.37}Ti_{0.94}Rh_{0.06}O_{3-\delta}$ (5.89 Ω cm² at 850 °C) [66] and $Sm_{0.70}Sr_{0.20}Fe_{0.80}Ti_{0.15}Ru_{0.05}O_{3-\delta}$ (0.13 Ω cm² at 800 °C) [67].

In hydrogen atmosphere, the screen-printed electrode with composition 50SPTO-PM exhibits R_p values of 7.42 Ω cm² at 650 °C, which are drastically reduced for the nanocomposite electrodes (Fig. 7b). The lowest polarization resistance is achieved for 50SPTO, 0.72 Ω cm² at 650 °C compared to 1.53 and 1.98 Ω cm² for 40SPTO and 60SPTO, respectively. The corresponding activation energies take a minimum value of 0.79 eV for 50SPTO and, as expected, they are lower than those obtained in air due to the sluggish ORR kinetics compared to HOR.

In general, these polarization resistance values are competitive compared to another symmetrical electrodes operating in H_2

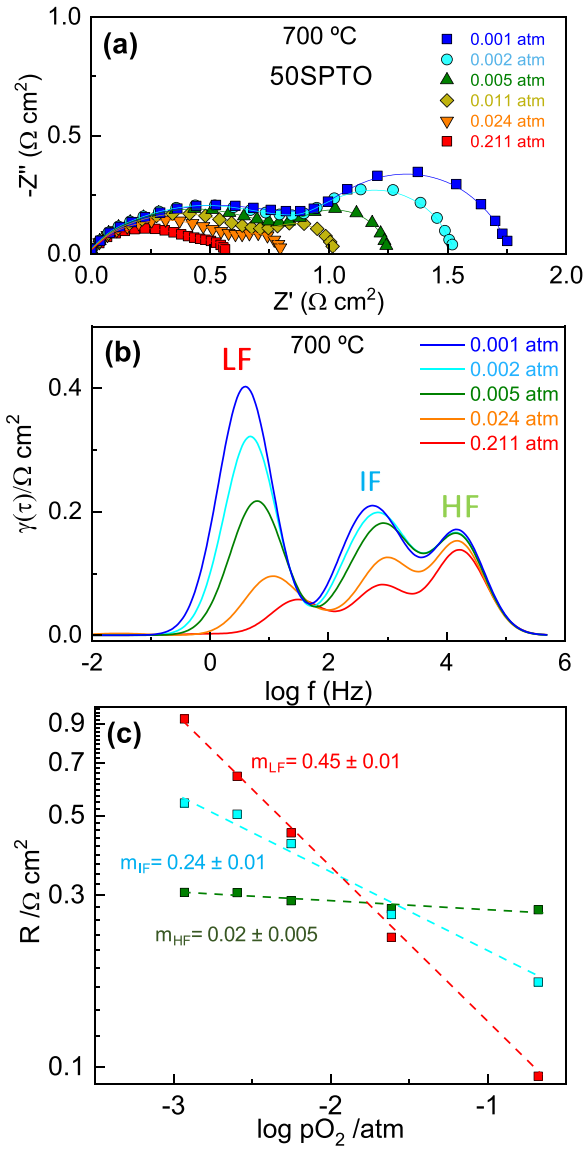

Fig. 6. (a) Impedance spectra of 50SPTO measured at different oxygen partial pressures at 700 ºC, (b) the corresponding DRT spectra and (c) polarization resistance of the different electrochemical processes as a function of pO_2.

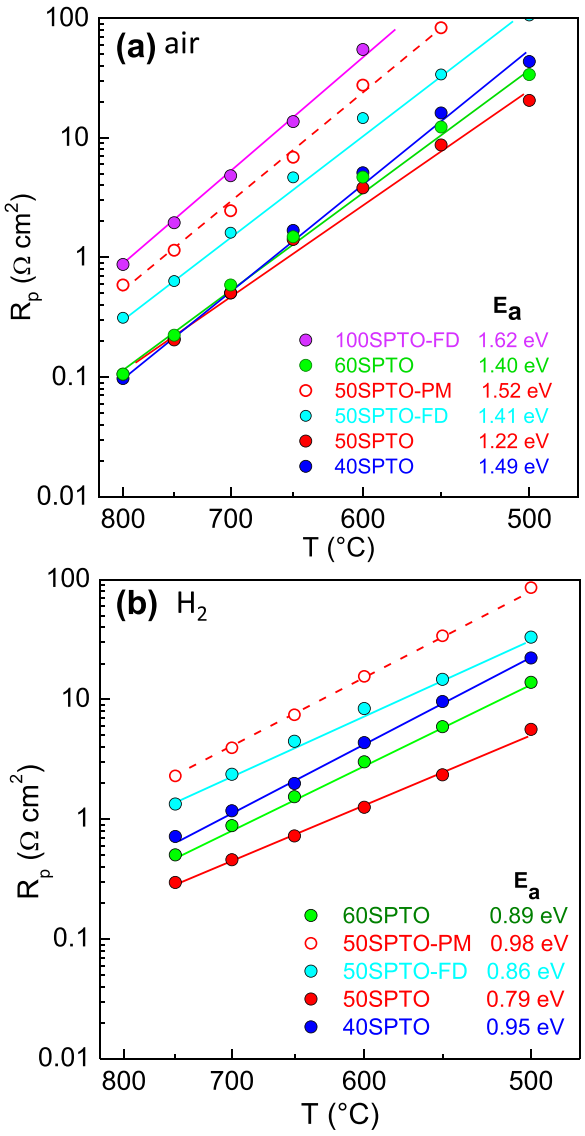

Fig. 7. Total polarization resistance of the symmetrical cells in (a) air and (b) H_2.

atmosphere, such as $La_{0.75}Sr_{0.25}Cr_{0.5}Mn_{0.5}O_{3-\delta}$ (1.82 Ω cm^2 at 850 ºC) [68], $PrBaFe_2O_{5+\delta}$ (0.9 Ω cm^2 at 650 ºC) [9] and $Sr_2Fe_{1.5}Mo_{0.5}O_{6-\delta}$ (0.45 Ω cm^2 at 800 ºC) [8] or even titanate-based anode materials with highly active exsolved metal nanoparticles, e.g. $(Sr_{0.94}Ti_{0.9}Nb_{0.1})_{0.95}Ni_{0.05}O_{3-\delta}$ (7.0 Ω cm^2 at 750 ºC) [28], $La_{0.2}Sr_{0.8}Ti_{0.9}Ni_{0.1}O_{3-\delta}$ (1.66 Ω cm^2 at 800 ºC) [69] and $La_{0.4}Sr_{0.6}Ti_{0.95}Ru_{0.05}O_{3-\delta}$ (2.74 Ω cm^2 at 850 ºC) [70] (Table 1).

3.5. Fuel cell test

The efficiency of the electrodes was evaluated under real operation conditions in a symmetrical cell: 50SPTO / LSGM(300 µm) / 50SPTO. Figs. 8a and 8b compare the current-voltage and power density curves of 50SPTO deposited by screen-printing and spray-pyrolysis, respectively. The open circuit voltage for both cells is close to the theoretical Nernst potential (1.1 V), confirming a good sealing of the cell. The cell with screen-printed electrodes reaches maximum power densities of 125, 70 and 40 mW cm^{-2} at 800, 750 and 700 ºC, respectively (Fig. 8a). These values are significantly improved for the nanocomposite electrode prepared by spray-pyrolysis, i.e. 354, 250 and 170 mW cm^{-2} at 800, 750 and 700 ºC, respectively (Fig. 8b). Moreover, the cell voltage at a constant current of 0.4 A cm^{-2} remains stable over time at 0.83 V for over 140 h of continuous operation in hydrogen at 800 ºC (Fig. 8c) without appreciable performance degradation or delamination of the cell components (Fig. 8d), confirming a good stability of the nanocomposite electrodes. These values of power density are higher than those previously reported for related $SrTiO_3$-based anode materials (Table 1). For instance, 170 mW cm^{-2} at 800 ºC for $La_{0.4}Sr_{0.4}TiO_3$-CGO/LSGM/LSCF-CGO [26] and 200 mW cm^{-2} at 900 ºC for $Sr_{0.89}Y_{0.07}TiO_{3-\delta}$-YSZ/YSZ/LSM-YSZ [71].

It has to be also commented that the performance of these nanocomposite electrodes is mainly limited by their poor electrical conductivity, especially in oxidizing atmosphere. Thus, alternative compositions could be prepared by partially substituting Ti for more reducible transition metal cations, such as Fe, Co and Ni. For instance, the incorporation of a little amount of Ni in the B-site of the perovskite structure would result in better properties in reducing atmosphere due to Ni-exsolution without compromising the structural stability and durability of these electrodes [72].

In summary, the design of novel nanostructured composite electrodes based on $SrTiO_3$-CeO_2 system is a promising approach to obtain

Table 1
Electrochemical properties of several $SrTiO_3$ −based anodes and symmetrical electrodes. Polarization resistance values (R_p) in H_2 and maximum power densities are given at 800 °C. The temperature is included when data are not available at 800 °C. The materials tested as symmetrical electrodes are indicated with an asterisk.

Anode	Cathode	R_p H_2 (Ω cm^2)	Electrolyte	Power density (mW cm^{-2})	Ref
50SPTO-PM*	50SPTO-PM	$3.94^{700\ °C}$	LSGM (300 μm)	125	This work
50SPTO*	50SPTO	$0.46^{700\ °C}$	LSGM (300 μm)	354	This work
$La_{0.3}Sr_{0.6}TiO_3$-YSZ	LSM/YSZ	$0.66^{850\ °C}$	YSZ (400 μm)	75	[73]
$La_{0.4}Sr_{0.4}TiO_3$-CGO	LSCF-CGO	–	LSGM (300 μm)	170	[26]
$La_{0.2}Sr_{0.8}TiO_3$-CGO	BSCF	3.4	LSGM (500 μm)	60	[74]
$La_{0.2}Sr_{0.8}TiO_3$-CGO	LSCF	2.1	LSGM (600 μm)	67	[75]
$La_{0.2}Sr_{0.25}Ca_{0.45}TiO_3$	LSM/YSZ	–	ScSZ (160 μm)	$290^{900\ °C}$	[76]
$La_{0.3}Sr_{0.7}Ti_{0.97}Mo_{0.03}O_3$	BSCF	$5.0^{850\ °C}$	LSGM (400 μm)	60	[77]
$Sr_{0.88}Y_{0.08}TiO_3$-$La_{0.4}Ce_{0.6}O_{1.8}$	SSC	–	LSGM (300 μm)	229	[78]
$Sr_{0.89}Y_{0.07}TiO_{3-\delta}$-YSZ	LSM/YSZ	–	YSZ (300 μm)	$200^{900\ °C}$	[71]
$CaTi_{0.6}Fe_{0.4}O_{3-\delta}$*	$CaTi_{0.6}Fe_{0.4}O_{3-\delta}$	1.0	YSZ (300 μm)	58	[25]
$SrTi_{0.9}Nb_{0.1}O_{3-\delta}$	LSM/CGO	$5.7^{850\ °C}$	ScSZ (500 μm)	$300^{850°C}$	[28]
$La_{0.4}Sr_{0.4}Ti_{0.9}Ni_{0.1}O_3$	LSCF/CGO	0.5	ScSZ (300 μm)	225	[79]
$La_{0.4}Sr_{0.6}Ti_{0.95}Ru_{0.05}O_{3-\delta}$-YSZ	LSM-YSZ	$2.5^{850\ °C}$	YSZ (800 μm)	$115^{850\ °C}$	[70]
$La_{0.5}Sr_{0.5}Ti_{0.5}Co_{0.5}O_{3-\delta}$ (LSTC)*	LSTC	–	LSGM (300 μm)	110	[80]

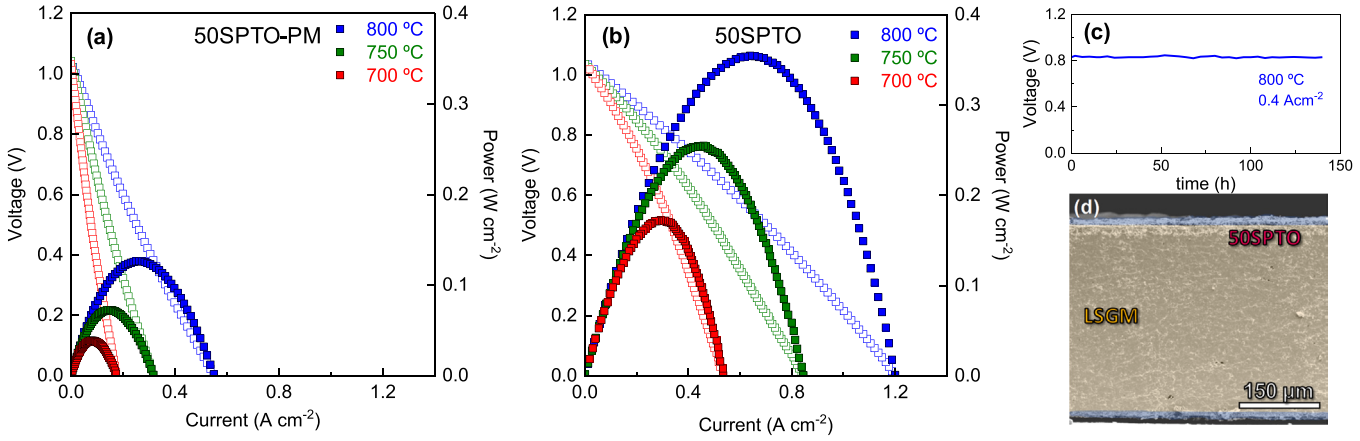

Fig. 8. Current-voltage and power density curves of LSGM supported cells with 50SPTO electrode deposited by (a) screen-printing and (b) spray-pyrolysis. (c) Durability test of the cell with 50SPTO deposited by spray-pyrolysis at a constant current density of 0.4 A cm^{-2} at 800 °C. (d) Cross-sectional SEM image of the cell after the durability test.

highly efficient and durable fuel and air electrodes for application in SOFC and electrolyzers. However, the deposition temperature needs to be sufficiently low to obtain a highly porous microstructure with larger TPB density. In this context, spray-pyrolysis deposition guarantees improved adherence of the electrodes to the electrolyte and enhanced electrocatalytic activity due to the lower preparation temperature.

4. Conclusions

Nanocomposite electrodes with composition $x(Sr_{0.7}Pr_{0.3})_{0.95}TiO_3$ – (100-x)$Ce_{0.9}Gd_{0.1}O_{1.95}$ (x = 0–60 wt%) (xSPTO) were successfully prepared by different methods: (i) spray-pyrolysis deposition in one-step on the electrolyte surface at 450 °C and traditional screen-printed method at 1100 °C by (ii) physically mixed powders and (iii) co-synthesis powders via a freeze-drying method.

The phase formation of the nanocomposite electrodes was confirmed by XRD and TEM analysis. SPTO crystallized with a single cubic perovskite structure when the sintering temperature was limited below 800 °C; however, extended ordered defects were observed at 1000 °C, which are reported to be detrimental for the electrochemical properties.

The microstructural analysis revealed that the co-synthesis of both SPTO and CGO phases inhibited the grain growth, retaining a nanometric grain size smaller than 60 nm at 1100 °C. In contrast, the electrodes prepared by traditional mixing powders and screen-printed deposition exhibited larger grain size ~450 nm at the same sintering temperature.

The electrodes directly assembled on the electrolyte surface achieved improved performance with polarization resistance values at 700 °C of 0.50 and 0.46 Ω cm^2 in air and pure H_2, respectively, much lower than those found for the screen-printed electrodes. The improved performance was explained by a reduction in the sintering steps and an intimate nanoscale contact between SPTO and CGO, which are beneficial to greatly improve the electrocatalytic activity in both oxidizing and reducing conditions without comprising the long-term stability upon redox cycling. Furthermore, the nanocomposite electrodes exhibited faster reduction kinetics compared to the bulk materials. A symmetrical cell with 50SPTO/LSGM/50SPTO configuration rendered a maximum power output of 354 mW cm^{-2} at 800 °C with negligible degradation for 140 h. These results demonstrated that the electrochemical performance of $SrTiO_3$ can be greatly enhanced by tailoring the microstructure at nanometric scale.

Declaration of Competing Interest

The authors declare that they have no known competing financial interests or personal relationships that could have appeared to influence the work reported in this paper.

Acknowledgements

This work was funded by PID2021–126009OB-I00 and PID2019–110249RB-I00 (Ministerio de Ciencia, Innovación y Universidades) and UMA18-FEDERJA-033 (Junta de Andalucia, Spain/FEDER) research projects. JZG thanks the Ministerio de Ciencia, Innovación y Universidades for his FPU grant (FPU17/02621) and Funding for open access charge: Universidad de Málaga/CBUA..

Appendix A. Supporting information

Supplementary data associated with this article can be found in the online version at doi:10.1016/j.jeurceramsoc.2022.11.059.

References

[1] T.M. Gür, Review of electrical energy storage technologies, materials and systems: challenges and prospects for large-scale grid storage, Energy Environ. Sci. 11 (2018) 2696–2767, https://doi.org/10.1039/c8ee01419a.
[2] Q. Xu, Z. Guo, L. Xia, Q. He, Z. Li, I. Temitope Bello, K. Zheng, M. Ni, A comprehensive review of solid oxide fuel cells operating on various promising alternative fuels, Energy Convers. Manag 253 (2022), 115175, https://doi.org/10.1016/j.enconman.2021.115175.
[3] M. Rafique, H. Nawaz, M. Shahid Rafique, M. Bilal Tahir, G. Nabi, N.R. Khalid, Material and method selection for efficient solid oxide fuel cell anode: Recent advancements and reviews, Int. J. Energy Res 43 (2019) 2423–2446, https://doi.org/10.1002/er.4210.
[4] B. Shri Prakash, S. Senthil Kumar, S.T. Aruna, Properties and development of Ni/YSZ as an anode material in solid oxide fuel cell: A review, Renew. Sustain. Energy Rev. 36 (2014) 149–179, https://doi.org/10.1016/j.rser.2014.04.043.
[5] J.C. Ruiz-Morales, J. Canales-Vázquez, J. Peña-Martínez, D. Marrero-López, P. Núñez, On the simultaneous use of $La_{0.75}Sr_{0.25}Cr_{0.5}Mn_{0.5}O_{3-\delta}$ as both anode and cathode material with improved microstructure in solid oxide fuel cells, Electrochim. Acta 52 (2006) 278–284, https://doi.org/10.1016/j.electacta.2006.05.006.
[6] D. Marrero-López, J. Peña-Martínez, J.C. Ruiz-Morales, M. Gabás, P. Núñez, M.A. G. Aranda, J.R. Ramos-Barrado, Redox behaviour, chemical compatibility and electrochemical performance of $Sr_2MgMoO_{6-\delta}$ as SOFC anode, Solid State Ion. 180 (2010) 1672–1682, https://doi.org/10.1016/j.ssi.2009.11.005.
[7] Y.-H. Huang, R.I. Dass, Z.-L. Xing, J.B. Goodenough, Double perovskites as anode materials for solid-oxide fuel cells, Science 312 (2006) 254–258, https://doi.org/10.1126/science.1125877.
[8] Q. Liu, X. Dong, G. Xiao, F. Zhao, F. Chen, A novel electrode material for symmetrical SOFCs, Adv. Mater. 22 (2010) 5478–5482, https://doi.org/10.1002/adma.201001044.
[9] B. Zhang, Y. Wan, Z. Hua, K. Tang, C. Xia, Tungsten-doped $PrBaFe_2O_{5+\delta}$ double perovskite as a high-performance electrode material for symmetrical solid oxide fuel cells, ACS Appl. Energy Mater. 4 (2021) 8401–8409, https://doi.org/10.1021/acsaem.1c01618.
[10] J. Zamudio-García, L. Caizán-Juanarena, J.M. Porras-Vázquez, E.R. Losilla, D. Marrero-López, A review on recent advances and trends in symmetrical electrodes for solid oxide cells, J. Power Sources 520 (2022), https://doi.org/10.1016/j.jpowsour.2021.230852.
[11] J.J. Alvarado Flores, M.L. Ávalos Rodríguez, G. Andrade Espinosa, J.V. Alcaraz Vera, Advances in the development of titanates for anodes in SOFC, Int. J. Hydrog. Energy 4 (2019) 12529–12542, https://doi.org/10.1016/j.ijhydene.2018.05.171.
[12] M.C. Verbraeken, T. Ramos, K. Agersted, Q. Ma, C.D. Savaniu, B.R. Sudireddy, J.T. S. Irvine, P. Holtappels, F. Tietz, Modified strontium titanates: From defect chemistry to SOFC anodes, RSC Adv. 5 (2015) 1168–1180, https://doi.org/10.1039/c4ra09751c.
[13] Z. Gao, E.C. Miller, S.A. Barnett, A high power density intermediate-temperature solid oxide fuel cell with thin $(La_{0.9}Sr_{0.1})_{0.98}(Ga_{0.8}Mg_{0.2})O_{3-\delta}$ electrolyte and nano-scale anode, Adv. Funct. Mater. 24 (2014) 5703–5709, https://doi.org/10.1002/adfm.201400295.
[14] A.A. Yaremchenko, J. Macías, A.V. Kovalevsky, B.I. Arias-Serrano, J.R. Frade, Electrical conductivity and thermal expansion of Ln-substituted $SrTiO_3$ for solid oxide cell electrodes and interconnects: the effect of rare-earth cation size, J. Power Sources 474 (2020), 228531, https://doi.org/10.1016/j.jpowsour.2020.228531.
[15] C.D. Savaniu, J.T.S. Irvine, Reduction studies and evaluation of surface modified A-site deficient La-doped $SrTiO_3$ as anode material for IT-SOFCs, J. Mater. Chem. 19 (2009) 8119–8128, https://doi.org/10.1039/b912305a.
[16] E. Da Rosa Silva, M. Curi, J.V. Nicolini, J.G. Furtado, A.R. Secchi, H.C. Ferraz, Effect of doping concentration and sintering atmosphere on the microstructural and electrical characteristics of Y-doped $SrTiO_3$ perovskite anode for SOFC, Ceram. Int. 47 (2021) 13331–13338, https://doi.org/10.1016/j.ceramint.2021.01.189.
[17] D.B. Drasbæk, M.M. Welander, M.L. Traulsen, B.R. Sudireddy, P. Holtappels, R. A. Walker, Operando characterization of metallic and bimetallic electrocatalysts for SOFC fuel electrodes operating under internal methane reforming conditions, J. Mater. Chem. A 10 (2022) 5550–5560, https://doi.org/10.1039/d1ta07299d.
[18] J.C. Ruiz-Morales, J. Canales-Vázquez, C. Savaniu, D. Marrero-López, W. Zhou, J.T. S. Irvine, Disruption of extended defects in solid oxide fuel cell anodes for methane oxidation, Nature 439 (2006) 568–571, https://doi.org/10.1038/nature04438.
[19] J. Canales-Vázquez, M.J. Smith, J.T.S. Irvine, W. Zhou, Studies on the reorganization of extended defects with increasing n in the perovskite-based $La_4Sr_{n-4}Ti_nO_{3n+2}$ Series, Adv. Funct. Mater. 15 (2005) 1000–1008, https://doi.org/10.1002/adfm.200400362.
[20] T. Kolodiazhnyi, A. Petric, The applicability of Sr-deficient n-type $SrTiO_3$ for SOFC anodes, J. Electroceram. 15 (2005) 5–11, https://doi.org/10.1007/s10832-005-0375-7.
[21] A. Yaremchenko, S.G. Patrício, J.R. Frade, Thermochemical behavior and transport properties of Pr-substituted $SrTiO_3$ as potential solid oxide fuel cell anode, J. Power Sources 245 (2014) 557–569, https://doi.org/10.1016/j.jpowsour.2013.07.019.
[22] X. Wang, Q. Hu, L. Li, X. Lu, Effect of Pr substitution on structural and dielectric properties of $SrTiO_3$, J. Appl. Phys. 112 (2012), https://doi.org/10.1063/1.4747937.
[23] C. Arrivé, T. Delahaye, O. Joubert, G.H. Gauthier, Study of $(La,Sr)(Ti,Ni)O_{3-\delta}$ materials for symmetrical Solid Oxide Cell electrode - Part C: Electrical and electrochemical behavior, Ceram. Int. 46 (2020) 23442–23456, https://doi.org/10.1016/j.ceramint.2020.06.114.
[24] J. Canales-Vázquez, J.C. Ruiz-Morales, D. Marrero-López, J. Peña-Martínez, P. Núñez, P. Gómez-Romero, Fe-substituted $(La,Sr)TiO_3$ as potential electrodes for symmetrical fuel cells (SFCs), J. Power Sources 171 (2007) 552–557, https://doi.org/10.1016/j.jpowsour.2007.05.094.
[25] L. dos Santos-Gómez, J.M. Porras-Vázquez, E.R. Losilla, D. Marrero-López, P. R. Slater, Investigation of PO_4^{3-} oxyanion-doping on the properties of $CaFe_{0.4}Ti_{0.6}O_{3-\delta}$ for potential application as symmetrical electrodes for SOFCs, J. Alloy. Compd. 835 (2020), https://doi.org/10.1016/j.jallcom.2020.155437.
[26] K.J. Kim, T.H. Shin, K.T. Lee, A-site deficient $La_{0.4}Sr_{0.4}TiO_3$-$Ce_{0.9}Gd_{0.1}O_{1.95}$ composites as efficient and redox stable anodes for solid oxide fuel cells, J. Alloy. Compd. 787 (2019) 1143–1148, https://doi.org/10.1016/j.jallcom.2019.02.180.
[27] M.K. Rath, K.T. Lee, Properties and electrochemical performance of $Sr_{0.8}La_{0.2}TiO_{3-\delta}$-$Ce_{0.8}Gd_{0.2}O_{2-\delta}$ composite anodes for intermediate temperature solid oxide fuel cells, J. Alloy. Compd. 657 (2016) 537–545, https://doi.org/10.1016/j.jallcom.2015.10.171.
[28] Y. Zhang, Z. Yu, Y. Tao, J. Lu, Y. Liu, J. Shao, Insight into the Electrochemical Processes of the Titanate Electrode with in Situ Ni Exsolution for Solid Oxide Cells, ACS Appl. Energy Mater. 2 (2019) 4033–4044, https://doi.org/10.1021/acsaem.8b02269.
[29] S. Futamura, A. Muramoto, Y. Tachikawa, J. Matsuda, S.M. Lyth, Y. Shiratori, S. Taniguchi, K. Sasaki, SOFC anodes impregnated with noble metal catalyst nanoparticles for high fuel utilization, Int. J. Hydrog. Energy 44 (2019) 8502–8518, https://doi.org/10.1016/j.ijhydene.2019.01.223.
[30] L. dos Santos-Gómez, J.M. Porras-Vázquez, E.R. Losilla, F. Martín, J.R. Ramos-Barrado, D. Marrero-López, LSCF-CGO nanocomposite cathodes deposited in a single step by spray-pyrolysis, J. Eur. Ceram. Soc. 38 (2018) 1647–1653, https://doi.org/10.1016/j.jeurceramsoc.2017.10.010.
[31] L. dos Santos-Gómez, J. Zamudio-García, J.M. Porras-Vázquez, E.R. Losilla, D. Marrero-López, Highly efficient $La_{0.8}Sr_{0.2}MnO_{3-\delta}$ - $Ce_{0.9}Gd_{0.1}O_{1.95}$ nanocomposite cathodes for solid oxide fuel cells, Ceram. Int 44 (2018) 4961–4966, https://doi.org/10.1016/j.ceramint.2017.12.089.
[32] L. dos Santos-Gómez, J. Zamudio-García, J.M. Porras-Vázquez, E.R. Losilla, D. Marrero-López, Recent progress in nanostructured electrodes for solid oxide fuel cells deposited by spray pyrolysis, J. Power Sources 507 (2021), https://doi.org/10.1016/j.jpowsour.2021.230277.
[33] J. Zamudio-García, J.M. Porras-Vázquez, E.R. Losilla, D. Marrero-López, $LaCrO_3$–CeO_2 -based nanocomposite electrodes for efficient symmetrical solid oxide fuel cells, ACS Appl. Energy Mater. (2022), https://doi.org/10.1021/acsaem.1c04116.
[34] L. Fan, C. Wang, M. Chen, B. Zhu, Recent development of ceria-based (nano) composite materials for low temperature ceramic fuel cells and electrolyte-free fuel cells, J. Power Sources 234 (2013) 154–174, https://doi.org/10.1016/j.jpowsour.2013.01.138.
[35] R. Raza, B. Zhu, A. Rafique, M.R. Naqvi, P. Lund, Functional ceria-based nanocomposites for advanced low-temperature (300–600 °C) solid oxide fuel cell: a comprehensive review, Mater. Today Energy 15 (2020), https://doi.org/10.1016/j.mtener.2019.100373.
[36] X'Pert HighScore Plus Software, v3.0e, PANalytical B. V., Amelo, The Netherlands,2012, (n.d.).
[37] R.B.V.D. A.C. Larson, General Structure Analysis System (GSAS) Software LosAlamos National Lab (2004) Rep. No. LAUR-86–748, (n.d.).
[38] J.C.C. Abrantes, Estereologia, UIDM, ESTG; Polytechnic Institute of Viana do Castelo: Viana do Castelo, (n.d.).
[39] L. Dos Santos-Gómez, J.M. Porras-Vázquez, E.R. Losilla, D. Marrero-López, Improving the efficiency of layered perovskite cathodes by microstructural optimization, J. Mater. Chem. A. 5 (2017) 7896–7904, https://doi.org/10.1039/c6ta10946b.
[40] J. Zamudio-García, J.M. Porras-Vázquez, E.R. Losilla, D. Marrero-López, Efficient symmetrical electrodes based on $LaCrO_3$ via microstructural engineering, J. Eur. Ceram. Soc. 42 (2022) 181–192, https://doi.org/10.1016/j.jeurceramsoc.2021.09.059.
[41] T.H. Wan, M. Saccoccio, C. Chen, F. Ciucci, Influence of the discretization methods on the distribution of relaxation times deconvolution: implementing radial basis functions with DRTtools, Electrochim. Acta 184 (2015) 483–499, https://doi.org/10.1016/j.electacta.2015.09.097.

[42] R.D. Shannon, Revised effective ionic radii and systematic studies of interatomic distances in halides and chalcogenides, Acta Cryst. A32 (1976) 751–767, https://doi.org/10.1107/S0567739476001551.

[43] J. Pradhan, H.K. Mallick, M.P.K. Sahoo, A.K. Pattanaik, Enhanced optical and dielectric properties of rare-earth co-doped $SrTiO_3$ ceramics, J. Mater. Sci. Mater. Electron 32 (2021) 13837–13849, https://doi.org/10.1007/s10854-021-05959-7.

[44] Y. Zhou, Q. Wen, Z. Ren, H. Xie, S. Tao, W. Zhou, Gadolinium-doped strontium titanate for high-efficiency electromagnetic interference shielding, J. Alloy. Compd. 733 (2018) 33–39, https://doi.org/10.1016/j.jallcom.2017.10.289.

[45] D.J. Cumming, J.A. Kilner, S. Skinner, Structural properties of Ce-doped strontium titanate for fuel cell applications, J. Mater. Chem. 21 (2011) 5021–5026, https://doi.org/10.1039/c0jm03680c.

[46] B. Kamecki, T. Miruszewski, J. Karczewski, Structural and electrical transport properties of Pr-doped $SrTi_{0.93}Co_{0.07}O_{3-\delta}$ a novel SOEC fuel electrode materials, J. Electroceram. 42 (2019) 31–40, https://doi.org/10.1007/s10832-018-0143-0.

[47] F. Tietz, Thermal expansion of SOFC materials, Ion. (Kiel.) 5 (1999) 129–139, https://doi.org/10.1007/BF02375916.

[48] H. Shimada, Y. Fujimaki, Y. Fujishiro, Highly active and durable $La_{0.4}Sr_{0.6}MnO_{3-\delta}$ and $Ce_{0.8}Gd_{0.2}O_{1.9}$ nanocomposite electrode for high-temperature reversible solid oxide electrochemical cells, Ceram. Int 46 (2020) 19617–19623, https://doi.org/10.1016/j.ceramint.2020.05.030.

[49] A.A. Yaremchenko, E.N. Naumovich, S.G. Patrício, O.V. Merkulov, M.V. Patrakeev, J.R. Frade, Rare-earth-substituted strontium titanate: insight into local oxygen-rich structures and redox kinetics, Inorg. Chem. 55 (2016) 4836–4849, https://doi.org/10.1021/acs.inorgchem.6b00350.

[50] T. Shi, Y. Chen, X. Guo, Defect chemistry of alkaline earth metal (Sr/Ba) titanates, Prog. Mater. Sci. 80 (2016) 77–132, https://doi.org/10.1016/j.pmatsci.2015.10.002.

[51] D.A. Osinkin, An approach to the analysis of the impedance spectra of solid oxide fuel cell using the DRT technique, Electrochim. Acta 372 (2021), 137858, https://doi.org/10.1016/j.electacta.2021.137858.

[52] J. Xia, C. Wang, X. Wang, L. Bi, Y. Zhang, A perspective on DRT applications for the analysis of solid oxide cell electrodes, Electrochim. Acta 349 (2020), 136328, https://doi.org/10.1016/j.electacta.2020.136328.

[53] D.A. Osinkin, Detailed analysis of electrochemical behavior of high–performance solid oxide fuel cell using DRT technique, J. Power Sources 527 (2022), 231120, https://doi.org/10.1016/j.jpowsour.2022.231120.

[54] Y. Chen, Y. Bu, Y. Zhang, R. Yan, D. Ding, B. Zhao, S. Yoo, D. Dang, R. Hu, C. Yang, M. Liu, A highly efficient and robust nanofiber cathode for solid oxide fuel cells, Adv. Energy Mater. 7 (2017) 1–7, https://doi.org/10.1002/aenm.201601890.

[55] H. Sumi, H. Shimada, Y. Yamaguchi, T. Yamaguchi, Y. Fujishiro, Degradation evaluation by distribution of relaxation times analysis for microtubular solid oxide fuel cells, Electrochim. Acta 339 (2020), 135913, https://doi.org/10.1016/j.electacta.2020.135913.

[56] J. Zamudio-García, L. Caizán-Juanarena, J.M. Porras-Vázquez, E.R. Losilla, D. Marrero-lópez, Boosting the performance of $La_{0.8}Sr_{0.2}MnO_{3-d}$ electrodes by the incorporation of nanocomposite active layers, Adv. Mat. Interfaces 9 (2022) 2200702, https://doi.org/10.1002/admi.202200702.

[57] Z. He, N. Ai, S. He, S.P. Jiang, L. Zhang, W.D.A. Rickard, D. Tang, K. Chen, Positive effect of incorporating $Er_{0.4}Bi_{1.6}O_3$ on the performance and stability of $La_2NiO_{4+\delta}$ cathode, J. Electrochem. Soc. 166 (2019) F796–F804, https://doi.org/10.1149/2.0841912jes.

[58] L. Almar, J. Szász, A. Weber, E. Ivers-Tiffée, Oxygen transport kinetics of mixed ionic-electronic conductors by coupling focused ion beam tomography and electrochemical impedance spectroscopy, J. Electrochem. Soc. 164 (2017) F289–F297, https://doi.org/10.1149/2.0851704jes.

[59] S.B. Adler, Mechanism and kinetics of oxygen reduction on porous $La_{1-x}Sr_xCoO_{3-\delta}$ electrodes, Solid State Ion. 111 (1998) 125–134, https://doi.org/10.1016/s0167-2738(98)00179-9.

[60] E. Siebert, A. Hammouche, M. Kleitz, Impedance spectroscopy analysis of $La_{1-x}Sr_{itx}MnO_3$-yttria-stabilized zirconia electrode kinetics, Electrochim. Acta 40 (1995) 1741–1753, https://doi.org/10.1016/0013-4686(94)00361-4.

[61] Y. Zhang, L. Shen, Y. Wang, Z. Du, B. Zhang, F. Ciucci, H. Zhao, Enhanced oxygen reduction kinetics of IT-SOFC cathode with $PrBaCo_2O_{5+\delta}/Gd_{0.1}Ce_{1.9}O_{2-\delta}$ coherent interface, J. Mater. Chem. A 10 (2022) 3495–3505, https://doi.org/10.1039/d1ta09615j.

[62] X. Kuai, G. Yang, Y. Chen, H. Sun, J. Dai, Y. Song, R. Ran, W. Wang, W. Zhou, Z. Shao, Boosting the activity of $BaCo_{0.4}Fe_{0.4}Zr_{0.1}Y_{0.1}O_{3-\delta}$ perovskite for oxygen reduction reactions at low-to-intermediate temperatures through tuning B-site cation deficiency, Adv. Energy Mater. 9 (2019) 1–11, https://doi.org/10.1002/aenm.201902384.

[63] X.J. Chen, K.A. Khor, S.H. Chan, Identification of O_2 reduction processes at yttria stabilized zirconia=doped lanthanum manganite interface, J. Power Sources 123 (2003) 17–25, https://doi.org/10.1016/S0378-7753(03)00436-1.

[64] J. Zhang, L. Lei, H. Li, F. Chen, M. Han, A practical approach for identifying various polarization behaviors of redox-stable electrodes in symmetrical solid oxide fuel cells, Electrochim. Acta 384 (2021), 138340, https://doi.org/10.1016/j.electacta.2021.138340.

[65] D. Marrero-López, L. Dos Santos-Gómez, J. Canales-Vázquez, F. Martín, J. R. Ramos-Barrado, Stability and performance of nanostructured $La_{0.8}Sr_{0.2}MnO_3$ cathodes deposited by spray-pyrolysis, Electrochim. Acta 134 (2014) 159–166, https://doi.org/10.1016/j.electacta.2014.04.154.

[66] V. Kyriakou, D. Neagu, G. Zafeiropoulos, R.K. Sharma, C. Tang, K. Kousi, I. S. Metcalfe, M.C.M. Van De Sanden, M.N. Tsampas, Symmetrical exsolution of Rh nanoparticles in solid oxide cells for efficient syngas production from greenhouse gases, ACS Catal. 10 (2020) 1278–1288, https://doi.org/10.1021/acscatal.9b04424.

[67] W. Fan, Z. Sun, Y. Bai, K. Wu, J. Zhou, Y. Cheng, In situ growth of nanoparticles in A-site deficient ferrite perovskite as an advanced electrode for symmetrical solid oxide fuel cells, J. Power Sources 456 (2020), 228000, https://doi.org/10.1016/j.jpowsour.2020.228000.

[68] I. Jung, D. Lee, S.O. Lee, D. Kim, J. Kim, S.H. Hyun, J. Moon, LSCM-YSZ nanocomposites for a high performance SOFC anode, Ceram. Int. 39 (2013) 9753–9758, https://doi.org/10.1016/j.ceramint.2013.05.022.

[69] B.H. Park, G.M. Choi, Ex-solution of Ni nanoparticles in a $La_{0.2}Sr_{0.8}Ti_{1-x}Ni_xO_{3-\delta}$ alternative anode for solid oxide fuel cell, Solid State Ion. 262 (2014) 345–348, https://doi.org/10.1016/j.ssi.2013.10.016.

[70] H. Yoon, J. Zou, N.M. Sammes, J. Chung, Ru-doped lanthanum strontium titanates for the anode of solid oxide fuel cells, Int. J. Hydrog. Energy 40 (2015) 10985–10993, https://doi.org/10.1016/j.ijhydene.2015.05.193.

[71] L. Shao, F. Si, X.Z. Fu, J.L. Luo, Archiving high-performance solid oxide fuel cells with titanate anode in sulfur- and carbon-containing fuels, Electrochim. Acta 270 (2018) 9–13, https://doi.org/10.1016/j.electacta.2018.03.078.

[72] O. Korjus, P. Möller, K. Kooser, T. Käämbre, O. Volobujeva, J. Nerut, S. Kotkas, E. Lust, G. Nurk, Influence of Ni concentration on electrochemical and crystallographic properties of $La_{0.25}Sr_{0.25}Ca_{0.4}Ti_{1-x}Ni_xO_{3-\delta}$ solid oxide fuel cell anode, J. Power Sources 494 (2021), https://doi.org/10.1016/j.jpowsour.2021.229739.

[73] J. Cheng, J. Gong, S. Yue, Y. Jiang, X. Hou, J. Ma, Y. Yao, C. Jiang, Electrochemical investigation of $La_{0.4}Sr_{0.6}TiO_3$ synthesized in air for SOFC application, J. Appl. Electrochem 51 (2021) 1175–1188, https://doi.org/10.1007/s10800-021-01568-8.

[74] K. Bin Yoo, G.M. Choi, Performance of La-doped strontium titanate (LST) anode on $LaGaO_3$-based SOFC, Solid State Ion. 180 (2009) 867–871, https://doi.org/10.1016/j.ssi.2009.02.013.

[75] K. Bin Yoo, G.M. Choi, LST-GDC composite anode on $LaGaO_3$-based solid oxide fuel cell, Solid State Ion. 192 (2011) 515–518, https://doi.org/10.1016/j.ssi.2010.06.048.

[76] M.C. Verbraeken, B. Iwanschitz, A. Mai, J.T.S. Irvine, Evaluation of Ca Doped $La_{0.2}Sr_{0.7}TiO_3$ as an Alternative Material for Use in SOFC Anodes, J. Electrochem. Soc. 159 (2012) F757–F762, https://doi.org/10.1149/2.001212jes.

[77] J. Li, T. Lv, N. Hou, P. Li, X. Yao, L. Fan, T. Gan, Y. Zhao, Y. Li, Molybdenum substitution at the B-site of lanthanum strontium titanate anodes for solid oxide fuel cells, Int. J. Hydrog. Energy 42 (2017) 22294–22301, https://doi.org/10.1016/j.ijhydene.2017.03.189.

[78] X.C. Lu, J.H. Zhu, Z. Yang, G. Xia, J.W. Stevenson, Pd-impregnated SYT/LDC composite as sulfur-tolerant anode for solid oxide fuel cells, J. Power Sources 192 (2009) 381–384, https://doi.org/10.1016/j.jpowsour.2009.03.009.

[79] B.H. Park, G.M. Choi, Electrochemical performance and stability of $La_{0.2}Sr_{0.8}Ti_{0.9}Ni_{0.1}O_{3-\delta}$ and $La_{0.2}Sr_{0.8}Ti_{0.9}Ni_{0.1}O_{3-\delta}$ - $Gd_{0.2}Ce_{0.8}O_{2-\delta}$ anode with anode interlayer in H_2 and CH_4, Electrochim. Acta 182 (2015) 39–46, https://doi.org/10.1016/j.electacta.2015.09.017.

[80] R. Martínez-Coronado, A. Aguadero, D. Pérez-Coll, L. Troncoso, J.A. Alonso, M. T. Fernández-Díaz, Characterization of $La_{0.5}Sr_{0.5}Co_{0.5}Ti_{0.5}O_{3-\delta}$ as symmetrical electrode material for intermediate-temperature solid-oxide fuel cells, Int. J. Hydrog. Energy 37 (2012) 18310–18318, https://doi.org/10.1016/j.ijhydene.2012.09.033.